Chinese Journal of Natural Medicines

Discovery of dimeric costunolide–triazole conjugates as antihepatoma agents *via* integrating dimerization and molecular hybridization

Tianze Li, Chenxi Jiang, Qihao Li, Min–min Hu, Yabo Li, Yao Yang, Yunbao Ma, Yongcui Wang, Jijun Chen

Citation: Tianze Li, Chenxi Jiang, Qihao Li, Min–min Hu, Yabo Li, Yao Yang, Yunbao Ma, Yongcui Wang, Jijun Chen, Discovery of dimeric costunolide–triazole conjugates as antihepatoma agents *via* integrating dimerization and molecular hybridization, Chinese Journal of Natural Medicines, 2026, 24(8), 1006–1014. doi: 10.1016/S1875–5364(26)61098–9.

View online: https://doi.org/10.1016/S1875–5364(26)61098–9

Related articles that may interest you

Artemdubinoids A–N: novel sesquiterpenoids with antihepatoma cytotoxicity from *Artemisia dubia*

Chinese Journal of Natural Medicines. 2023, 21(12), 902–915 https://doi.org/10.1016/S1875–5364(23)60441–8

Anti–psoriasis molecular targets and active components discovery of Optimized Yinxieling Formula *via* affinity–purified strategy

Chinese Journal of Natural Medicines. 2024, 22(2), 127–136 https://doi.org/10.1016/S1875–5364(24)60563–7

Eudesmane–guaiane sesquiterpenoid dimers from *Aucklandia costus* trigger paraptosis–like cell death *via* ROS accumulation and MAPK hyperactivation

Chinese Journal of Natural Medicines. 2024, 22(11), 1011–1019 https://doi.org/10.1016/S1875–5364(24)60592–3

A systematic review of pharmacological activities, toxicological mechanisms and pharmacokinetic studies on *Aconitum* alkaloids

Chinese Journal of Natural Medicines. 2021, 19(7), 505–520 https://doi.org/10.1016/S1875–5364(21)60050–X

Deciphering chemical and metabolite profiling of Chang–Kang–Fang by UPLC–Q–TOF–MS/MS and its potential active components identification

Chinese Journal of Natural Medicines. 2023, 21(6), 459–480 https://doi.org/10.1016/S1875–5364(23)60474–1

The bioinformatics and metabolomics research on anti–hypoxic molecular mechanisms of Salidroside *via* regulating the PTEN mediated PI3K/Akt/NF–κB signaling pathway

Chinese Journal of Natural Medicines. 2021, 19(6), 442–453 https://doi.org/10.1016/S1875–5364(21)60043–2

Wechat

Chinese Journal of Natural Medicines 24 (2026) 1006-1014

Contents lists available at ScienceDirect

Chinese Journal of Natural Medicines

journal homepage: www.cjnmcpu.com/

Original article

Discovery of dimeric costunolide-triazole conjugates as antihepatoma agents *via* integrating dimerization and molecular hybridization

Tianze Li[a,Δ], Chenxi Jiang[a, b,Δ], Qihao Li[a, c], Min-min Hu[a, c], Yabo Li[a], Yao Yang[a, c], Yunbao Ma[a], Yongcui Wang[a], Jijun Chen[a, c,*]

[a] *Kunming Institute of Botany, Chinese Academy of Sciences, State Key Laboratory of Phytochemistry and Natural Medicines, Kunming 650201, China*

[b] *Key Laboratory of Applied Surface and Colloid Chemistry, Ministry of Education and School of Chemistry and Chemical Engineering, Shaanxi Normal University, Xi'an 710062, China*

[c] *Medical School, University of Chinese Academy of Sciences, Beijing 100049, China*

ARTICLE INFO

Article history:
Received 10 November 2025
Revised 14 December 2025
Accepted 28 January 2026
Available online 20 August 2026

Keywords:
Antihepatoma activity
Costunolide
Triazole
Dimers
Glucose-6-phosphate dehydrogenase (G6PD)
Mechanism

ABSTRACT

Costunolide, a natural germacranolide sesquiterpenoid, exhibits only moderate anti-HCC activity. To enhance its efficacy and tumor selectivity, a series of 37 dimeric costunolide-1,2,3-triazole conjugates was designed and synthesized by integrating dimerization and molecular hybridization strategies. Evaluation of their antiproliferative effects on HepG2, Huh-7, and SK-Hep-1 cells suggested that 25 compounds were more potent than either costunolide or sorafenib. The most active dimer **19** exhibited significant activity with IC_{50} values of 1.6, 1.3, and 0.7 μmol·L^{-1}, which were 13.1, 14.2, and 34.9-fold greater than those of costunolide. Compound **19** showed favorable selectivity against human normal liver cells (THLE-2) and markedly inhibited colony formation. Through a combination of bioinformatics, docking, and molecular dynamics (MD) simulations, glucose-6-phosphate dehydrogenase (G6PD) was identified as a target of compound **19**, which was subsequently validated by DARTS and SPR assays. Functional studies revealed that compound **19** arrested the HCC cell cycle at the G_2/M phase, suppressed migration and invasion by inhibiting epithelial-mesenchymal transition, and triggered both apoptosis and ferroptosis. These findings establish triazole-linked costunolide dimer **19** as a promising lead candidate for the development of novel anti-HCC therapies.

1. Introduction

Hepatocellular carcinoma (HCC) is the most common form of primary liver cancer and a leading cause of cancer-related mortality globally [1]. The applicability of surgical resection is limited to approximately 15% of patients, and the majority of patients with advanced disease rely on interventional, radiological, or systemic therapies. However, the efficacy of standard drug treatments -- such as tyrosine kinase inhibitors and immune checkpoint inhibitors -- is frequently limited by the development of chemoresistance [2]. Thus, there is an urgent need to develop new anti-HCC agents with novel structures and mechanisms of action.

Natural products represent a valuable resource for anticancer drug discovery [3]. Among them, costunolide, a germacranolide sesquiterpenoid isolated from *Saussurea costus*, has demonstrated antiproliferative effects in various cancer cell lines [4]. Its mechanisms include the induction of apoptosis, the suppression of telomerase activity, the blockade of angiogenesis, and the prevention of tumor metastasis [5]. Nevertheless, the clinical potential of costunolide is constrained by its moderate potency, off-target toxicity, and poor chemical and metabolic stability. Despite efforts to synthesize costunolide derivatives by modifying the *α*-methylene-*γ*-butyrolactone moiety [6-8], their antiproliferative activity remains modest.

Previous work from our group indicated that certain natural sesquiterpenoid dimers isolated from *Artemisia* species [9-14], along with their synthetic analogs [15, 16], exhibited significant antihepatoma activity by inhibiting cell migration and invasion, inducing apoptosis, and arresting the cell cycle. Dimerization is a recognized strategy to enhance the bioactivity of sesquiterpenoids *via* dual-target engagement or improved binding affinity. Indeed, dimeric sesquiterpenoids linked by esters [17-19], carbamates, carbonates [20] and all carbon linkers [21] have been synthesized and displayed potent antitumor properties. Molecular hybridization, the combination of two pharmacophores into one molecule, is another effective approach to optimize natural lead compounds [22]. In this context, the 1,2,3-triazole ring, which is easily accessible *via* copper-catalyzed azide-alkyne cycloaddition (CuAAC), serves as a privileged scaffold that can improve solubility and facilitate key biointeractions with target proteins [23, 24]. Previous studies have confirmed that hybrids of 1,2,3-triazole and sesquiterpenoids exhibit superb anticancer activity [25-27].

In our earlier investigation, costunolide showed moderate inhibitory effects on human HCC cell lines with IC_{50} values of 19.7 (HepG2), 16.5 (Huh-7), and 26.2 μmol·L^{-1} (SK -Hep-1) [16]. By in-

* Corresponding author.
E-mail address: chenjj@mail.kib.ac.cn (J. Chen)
Δ These authors contributed equally to this work.

https://doi.org/10.1016/S1875-5364(26)61098-9
Copyright © 2026, China Pharmaceutical University. Published by Elsevier B.V. All rights are reserved.

tegrating molecular hybridization and dimerization strategies, we hypothesized that tethering two costunolide units *via* a triazole-based linker could yield novel dimers with improved anti-HCC efficacy (Fig. 1). Compared with other linkers—such as esters, amides, or electrophilic groups—the 1,2,3-triazole linker offers distinct advantages, including more accessible synthesis and greater stability than traditional ester or amide bonds. In this study, we designed and synthesized a series of triazole-linked costunolide dimers from azide- and alkyne-functionalized precursors using a bis-click chemistry approach. Herein, we report the synthesis, antihepatoma activity, and mechanism investigation of these dimeric costunolide-1,2,3-triazole conjugates.

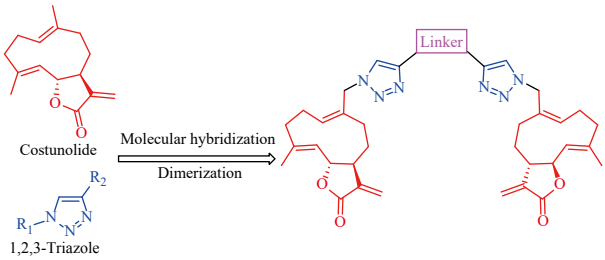


Fig. 1 Design of dimeric costunolide-1,2,3-triazole conjugates.

2. Results and discussion

2.1. Chemistry

Costunolide was obtained from *Saussurea costus* and converted to azide **A1** through a two-step sequence involving allylic oxidation and azidation using the DPPA–DBU method in 48% yield. Treatment of azide **A1** with various aromatic, heteroaromatic, and aliphatic diacetylenic compounds in the presence of $CuSO_4·5H_2O$ and sodium ascorbate in THF–H_2O (5∶1) at room temperature afforded the corresponding dimeric costunolide–1,2,3-triazole conjugates **1**–**31** and **34**–**37** (Scheme 1). The variation in the oxidation state at the sulfur atom of compound **31** using *m*-CPBA at different temperatures selectively provided sulfoxide **32** or sulfone **33**. The structures of the dimers were unambiguously characterized by ^{1}H NMR, ^{13}C NMR, and high-resolution mass spectrometry.

2.2. In vitro antihepatoma activity of the dimers

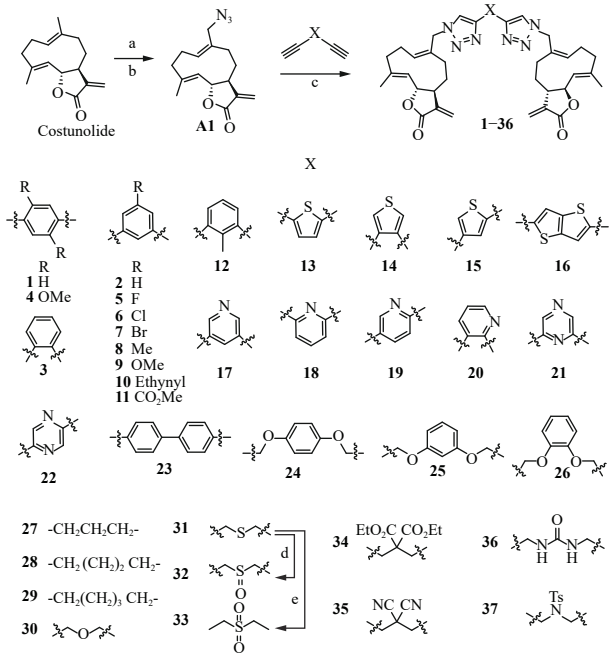
The antihepatoma activity of dimeric costunolide-1,2,3-triazole conjugates was evaluated in HepG2, Huh-7, and SK-Hep-1 cell lines *via* an MTT assay with sorafenib as a positive control. As summarized in Table 1, 25 compounds outperformed sorafenib and costunolide in inhibiting HepG2 cells, 27 dimers were more potent against Huh-7 cells, and 29 dimers showed enhanced activity against SK-Hep-1 cells. Notably, compounds **1**–**3**, **9**, **12**, **14**, **15**, **17**–**22**, **24**–**31**, **34**, **35**, and **37** consistently demonstrated stronger inhibition across all three cell lines than costunolide and sorafenib.

A comparison of phenyl-substituted compounds **1**–**3** and **24**–**26** revealed that *ortho*-substituted derivatives **3** and **26** consistently exhibited better activity than their *meta*- and *para*-substituted counterparts. The introduction of fluorine, chlorine, bromine, methyl, methoxy, ethynyl, or ester groups at the C-5′ position of compound **2** yielded compounds **5**–**11**, which resulted in a significant decrease in activity. The position of the methyl substituent on the benzene ring significantly influenced the potency, as the C-2′-substituted derivative **12** was more active than its C-5′-substituted isomer **8**.

The replacement of the phenyl ring with thiophene moieties identified 3,4-disubstituted derivative **14** as the most potent among analogs **13**–**15**, with IC_{50} values of 2.4 (HepG2), 2.3 (Huh-7), and 3.1 μmol·L^{-1} (SK-Hep-1). Pyridine-based analogues **17**–**20** universally demonstrated stronger inhibition than sorafenib, and 2,5-disubstituted compound **19** was the most active in the series with IC_{50} values of 1.6 (HepG2), 1.3 (Huh-7), and 0.7 μmol·L^{-1} (SK-Hep-1). Further expansion to the pyrazine ring afforded compounds **21** and **22** with comparable activities.

The antihepatoma activity of aliphatic derivatives **27**–**29** was correlated with chain length, and the four-carbon analogue **28** emerged as the most potent across all three cell lines. Among heteroatom-linked derivatives **30**–**33**, **36** and **37**, *p*-toluenesulfonamide-containing compound **37** was the most potent (IC_{50}: 1.8 μmol·L^{-1} for HepG2, 1.6 μmol·L^{-1} for Huh-7, 1.1 μmol·L^{-1} for SK-Hep-1). In contrast, the urea-linked derivative **36** showed markedly reduced activity. Compound **31** featuring a thioether linker was more potent than its ether-containing analog **30**, but oxidation of the sulfur in **31** to sulfone (**32**) or sulfoxide (**33**) led to a significant loss of activity. Finally, diester- and dicyano-substituted compounds **34** and **35** with IC_{50} values ranging from 1.3 to 5.6 μmol·L^{-1} displayed activities similar to those of compound **27**.

Compound **19** (KGA-1034) emerged as the most potent dimer with IC_{50} values of 1.6, 1.3, and 0.7 μmol·L^{-1} against HepG2, Huh-7, and SK-Hep-1 cells, respectively, which were 13.1, 14.2, and 34.9-fold higher than those of costunolide and 7.3, 6.1 and 20.6-fold more potent than those of sorafenib. The selectivity of compound **19**, costunolide and sorafenib against HCC cells over normal cells was studied by evaluating their cytotoxicity on the normal human liver cell line THLE-2. Costunolide showed equivalent toxicity to cancerous and normal cells (CC_{50}: 20.8 μmol·L^{-1}). While compound **19** demonstrated lower cytotoxicity on THLE2 (CC_{50}: 3.2 μmol·L^{-1}), indicating selectivity indices of 2.0, 2.5, and 4.6 against HepG2, Huh-7, and SK-Hep-1 cell lines, respectively. Sorafenib showed cytotoxic activity with a CC_{50} value of 20.6 μmol·L^{-1} with selectivity indices of 1.8, 2.6 and 1.4, respectively. These results indicated that the dimerization of costunolide *via* the triazole linker not only significantly increased its anti-HCC activity, but also improved tumor selectivity. Owing to its promising anti-HCC activity and favorable safety profile, com-



Scheme 1 Reagents and conditions for the synthesis of compounds **1**–**37**: (a) SeO_2, *t*-BuOOH, DCM, 0 °C–r.t.; (b) DPPA, DBU, THF, r.t.; (c) $CuSO_4·5H_2O$, sodium ascorbate, THF–H_2O, r.t.; (d) *m*-CPBA, DCM, 0 °C; (e) *m*-CPBA, DCM, 0 °C–r.t..

Table 1 Inhibitory activity of compounds **1**–**37** on HepG2, Huh-7 and SK-Hep-1 cells.

Compd.	IC_{50} (μmol·L^{-1})			Compd.	IC_{50} (μmol·L^{-1})		
	HepG2	Huh-7	SK-Hep-1		HepG2	Huh-7	SK-Hep-1
1	8.2	3.5	2.3	**21**	1.9	1.9	1.8
2	5.4	2.9	1.3	**22**	3.5	1.8	1.1
3	2.4	2.0	1.4	**23**	> 20	> 20	> 20
4	13.1	2.2	1.7	**24**	3.1	2.6	1.4
5	14.0	16.8	13.0	**25**	5.8	2.4	3.1
6	16.5	6.6	4.4	**26**	2.9	2.5	1.2
7	> 20	> 20	> 20	**27**	3.7	3.5	2.9
8	> 20	13.1	10.8	**28**	2.7	2.8	2.0
9	6.4	4.1	2.1	**29**	5.2	3.4	4.3
10	> 20	11.6	> 20	**30**	6.3	7.3	4.6
11	6.6	2.0	> 20	**31**	4.0	4.3	2.9
12	3.7	3.9	2.2	**32**	> 20	> 20	> 20
13	11.8	14.3	4.2	**33**	> 20	> 20	9.2
14	2.4	2.3	3.1	**34**	2.8	1.6	1.3
15	3.2	4.0	4.3	**35**	3.9	5.6	1.7
16	> 20	> 20	> 20	**36**	> 20	> 20	> 20
17	6.2	4.7	1.6	**37**	1.8	1.6	1.1
18	3.2	1.5	0.8	Costunolide	20.9	18.5	24.4
19	1.6	1.3	0.7	Sorafenib	11.7	8.0	14.4
20	1.8	1.2	1.3				

pound **19** was selected for further investigation of its preliminary mechanism of action.

*2.3. Compound **19** inhibited the colony formation of SK-Hep-1 and Huh-7 cells*

The antiproliferative potential of compound **19** was further evaluated through a colony formation assay. Over a 10-day period at different dosages, compound **19** obviously suppressed the colony-forming ability of SK-Hep-1 and Huh-7 cells in a concentration-dependent manner (Fig. 2). At concentrations of 0.3, 0.6, and 0.9 μmol·L^{-1}, the inhibitory ratios were 17.2%, 62.8%, and 92.9% for SK-Hep-1 cells, and 19.1%, 47.5%, and 81.6% for Huh-7 cells, respectively.

*2.4. Anti-HCC target analysis of compound **19***

To identify the protein targets of compound **19** in hepatocellular carcinoma, a multistep analysis was conducted. First, the CIPHEN (compound-protein interactions prediction based on the heterogeneous network) prediction model [28] was employed to identify the top 50 potential targets (Fig. 3A). Subsequent bioinformatic analysis of TCGA data revealed that 15 of these genes were differentially expressed in HCC *vs* normal tissues and were significantly correlated with patient survival (*P*-value < 0.05) (Fig. 3B). Finally, molecular docking was performed on this shortlist, indicating that compound **19** exhibited the most potent binding affinity for glucose-6-phosphate dehydrogenase (G6PD), with a docking score of −5.078 kcal·mol^{-1} (Fig. 3C). Specifically, the C-12 carbonyl group formed a hydrogen bond with Ser40, and the nitrogen atoms in the triazole ring formed hydrogen bonds with Asp-42 and Leu-43 (Fig. 3D).

Bioinformatics analysis revealed that G6PD expression was significantly upregulated in HCC tissues compared with adjacent normal tissues (Fig. 3E). It demonstrated considerable diagnostic value with an area under the ROC curve of approximately 0.95 for discriminating tumors from nontumorous samples (Fig. 3F). Furthermore, elevated G6PD expression was associated with advanced tumor stage and poorer overall survival (OS) (Figs. 3G and 3H). Previous studies indicated that G6PD promoted the proliferation, migration, and invasion of HCC cells [29]. Taken together, these findings establish G6PD as a clinically relevant therapeutic target in HCC.

To evaluate the binding stability and dynamic behavior of compound **19** with G6PD protein under simulated physiological conditions, molecular dynamics (MD) simulations were conducted. The root-mean-square deviation (RMSD) analysis indicated that the compound **19**–G6PD complex quickly reached equilibrium and maintained stable conformational dynamics throughout the simulation (Fig. 4A). Root-mean-square fluctuation (RMSF) plot showed that the G6PD protein and the complex exhibited similar flexibility for most residues (Fig. 4B). The radius of gyration (Rg) remained stable with only minor fluctuations, suggesting that the protein retained its structural integrity and compactness in both free and bound forms (Fig. 4C). Hydrogen bond analysis further confirmed intermolecular interactions between compound **19** and key residues in the G6PD active site (Fig. 4D). These findings demonstrated that G6PD and compound **19** formed a stable complex under physiological conditions.

To verify the interaction between compound **19** and G6PD, drug affinity responsive target stability (DARTS) and surface plasmon resonance (SPR) assays were performed. In both SK-Hep-1 and Huh-7 cells, increasing concentrations of compound **19** (from 0.5 to 1000 μmol·L^{-1}) resulted in a dose-dependent increase in the abundance of G6PD (Fig. 4E). This observation indicated that the binding of compound **19** stabilized G6PD and

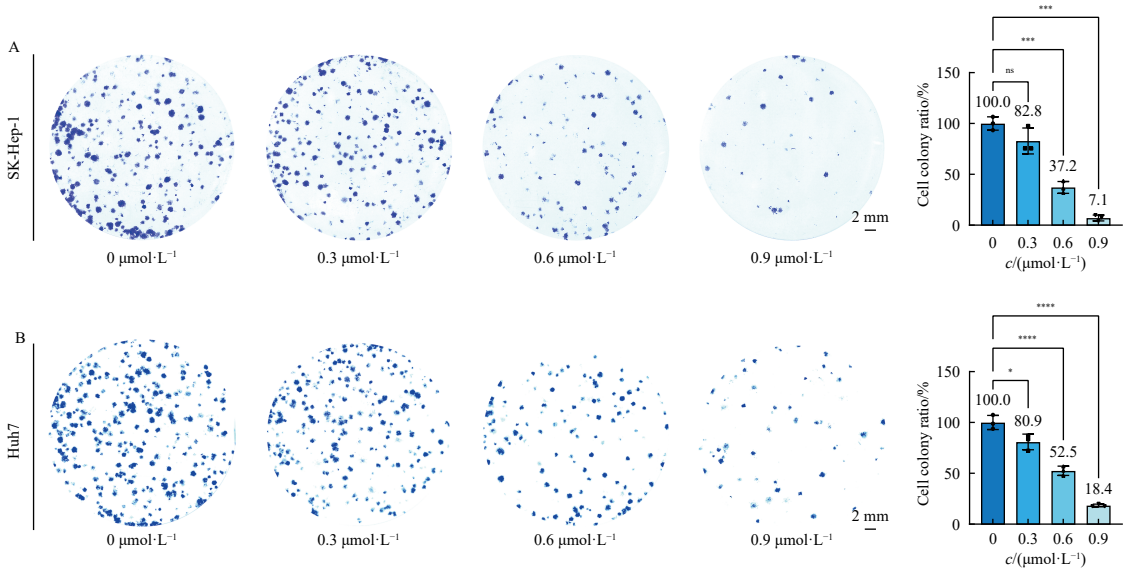


Fig. 2 Inhibitory effect of compound **19** on colony formation in SK-Hep-1 and Huh-7 cells (n = 3). (A) SK-Hep-1 cells. (B) Huh-7 cells. Data are presented as mean ± SD from three independent experiments. $^{*}P < 0.05$; $^{***}P < 0.001$; $^{****}P < 0.0001$

protected it from pronase degradation. Subsequent SPR analysis quantified this interaction to show that compound **19** had binding affinity with G6PD with a K_D value of 1.62 μmol·L^{-1} (Fig. 4F). These data collectively verify the direct binding between compound **19** and G6PD.

*2.5. Compound **19** suppressed the migration and invasion of SK-Hep-1 and Huh-7 cells*

Given the documented role of G6PD in promoting HCC metastasis through epithelial-mesenchymal transition (EMT) [30], the ef-

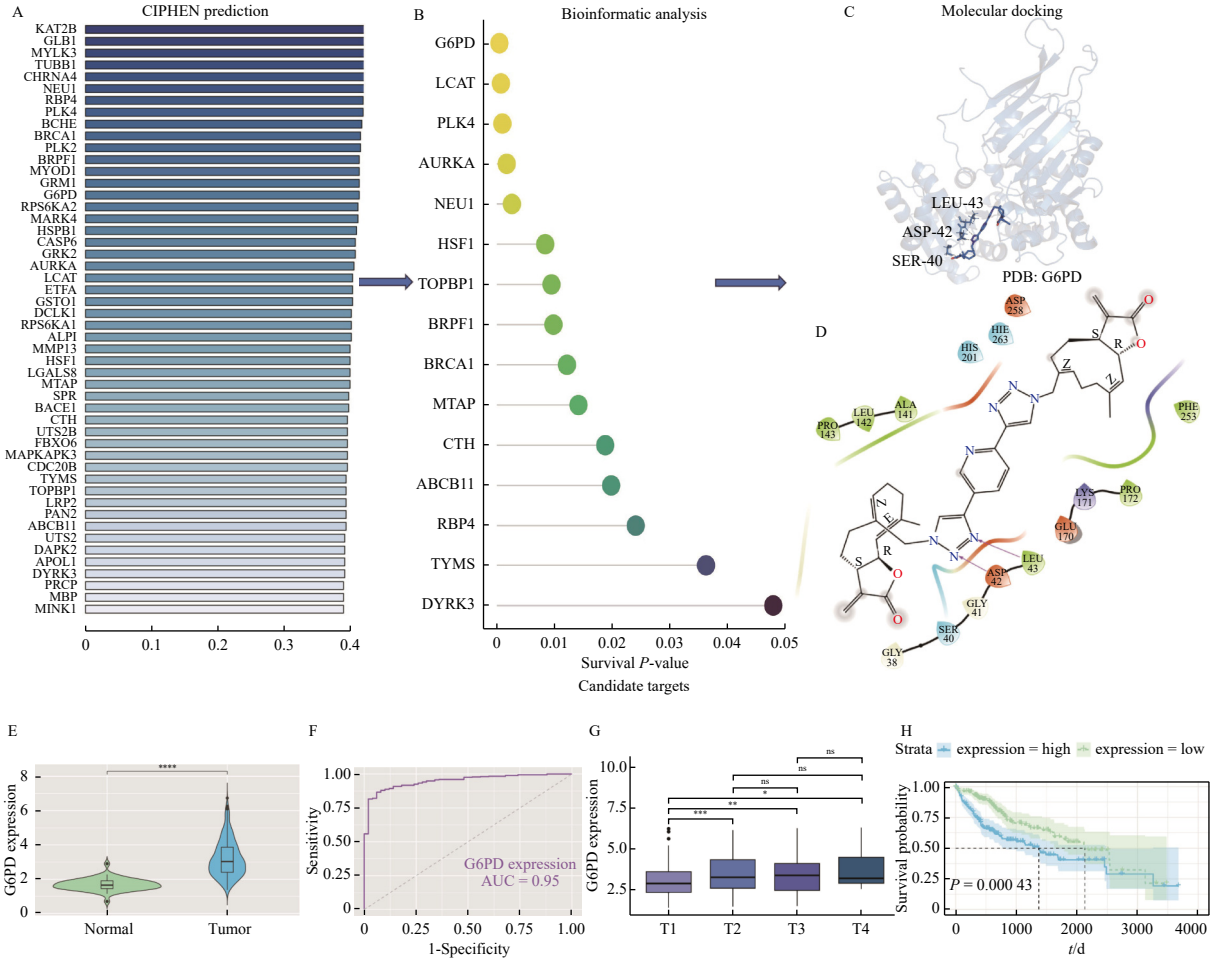


Fig. 3 Investigation of the target of compound **19**. (A) Prediction of the Top 50 potential targets of compound **19** using CIPHEN. (B) Screening of 15 candidate targets based on their expression in HCC tissues and correlation with patient survival. (C and D) Molecular docking analysis. (E) Expression levels of G6PD in liver tumors and adjacent normal tissues. (F) ROC curve of G6PD in LIHC. (G) G6PD expression across different tumor pathological stages in HCC patients. The number of patients in each stage was: T1, n = 183; T2, n = 95; T3, n = 80; T4, n = 13. (H) Survival analysis of HCC patients based on G6PD expression. $^{*}P < 0.05$; $^{**}P < 0.01$; $^{***}P < 0.001$; $^{****}P < 0.0001$.

fects of compound **19** on the migratory and invasive capabilities of SK-Hep-1 and Huh-7 cells were evaluated using a Transwell assay. As shown in Fig. 5A, compound **19** dose-dependently inhibited cell migration over 48 h as the number of migrated cells declining to 81.7%, 44.8%, and 9.1% of control in SK-Hep-1 cells and to 77.8%, 22.3%, and 10.5% in Huh-7 cells at 0.3, 0.6, and 0.9 μmol·L^{-1}, respectively. Similarly, the invasive capabilities of both SK-Hep-1 and Huh-7 cells were also markedly suppressed, with inhibitory ratios of 44.6% and 39.7% (0.3 μmol·L^{-1}), 90.9% and 55.4% (0.6 μmol·L^{-1}), and 97.6% and 82.8% (0.9 μmol·L^{-1}), respectively. Mechanistically, this anti-metastatic effect was associated with a reversal of EMT, as evidenced by the upregulation of *E*-cadherin and downregulation of *N*-cadherin and vimentin in SK-Hep-1 and Huh-7 cells upon compound **19** treatment (Fig. 5B).

*2.6. Compound **19** triggered G_2/M phase arrest in SK-Hep-1 and Huh-7 cells*

To further investigate the growth-inhibitory mechanisms of compound **19**, its effect on the cell cycle was examined in SK-Hep-1 and Huh-7 cells by flow cytometric analysis. Treatment with compound **19** (0.3, 0.6, and 0.9 μmol·L^{-1}) induced a concentration-dependent accumulation of cells in the G_2/M phase (Fig. 6A). In SK-Hep-1 cells, the G_2/M population was increased from 22.3% to 31.3%, 34.1%, and 38.9%; a similar increasement was observed in Huh-7 cells, from 19.4% to 22.6%, 29.4%, and 31.9%. Western blot analysis of key regulatory proteins indicated that the observed G_2/M phase arrest was associated with upregulated expression of Cyclin B1 and p21 (Fig. 6B).

*2.7. Compound **19** induced apoptosis and ferroptosis*

Given the known role of G6PD in regulating apoptosis [31] and ferroptosis [32], the potential of compound **19** to trigger these two forms of cell death was assessed. As shown in Fig 7A, treatment with compound **19** (0.3, 0.6, 0.9 μmol·L^{-1}) led to a concentration-dependent increase in the proportion of apoptotic/necrotic cells, as measured by Annexin V/PI staining. In SK-Hep-1 cells, the percentage was increased from 6.4% to 22.0%, 35.9%, and 72.6%; similarly, in Huh-7 cells, it increased from 3.3% to 11.0%, 29.4%, and 59.8%, indicating the induction of apoptosis in HCC cells. Given the pivotal roles of Bcl-2 (antiapoptotic) and Bax (proapoptotic) in mitochondrial apoptosis, the effects of compound **19** on their expression were examined. Western blot analysis revealed that compound **19** progressively upregulated Bax and downregulated Bcl-2 (Fig. 7B), demonstrating that it induced apoptosis through a mitochondrial pathway.

As reactive oxygen species (ROS) are a hallmark of ferroptosis, we assessed whether compound **19** triggers ferroptosis by measuring ROS levels *via* immunofluorescence (Fig. 7E). Compound **19** dose-dependently increased ROS levels in SK-Hep-1 cells. Importantly, this effect could be suppressed by the ferroptosis inhibitor ferrostatin-1 (Fer-1), suggesting that compound **19** could trigger ferroptosis in SK-Hep-1 cells.

3. Conclusions

Dimerization and molecular hybridization are effective strategies for enhancing the anticancer efficacy of sesquiterpenoids. In this work, a novel series of dimeric costunolide-1,2,3-triazole conjugates were designed, synthesized *via* a bis-click reaction, and assayed for their inhibitory effects on HepG2, Huh-7, and SK-Hep-1 cells. In total, 25 synthetic dimers were more active than sorafenib and costunolide across the three cell lines. Among them, compound **19** displayed excellent antiproliferative activity with IC_{50} values of 1.6 (HepG2), 1.3 (Huh-7), and 0.7 μmol·L^{-1} (SK-Hep-1), favorable selectivity against normal hepatocytes, and a marked ability to inhibit colony formation. Another significant finding of this work was the identification and experimental validation of G6PD as a direct target of compound **19**. This target engagement drives its multifaceted effects, including the inhibition of migration and invasion, cell cycle arrest, and the simultaneous induction of apoptosis and ferroptosis. Collectively, this research not only demonstrates the utility of combining dimerization with molecular hybridization but also establishes compound **19** as a promising lead for the development of novel anti-HCC therapeutics.

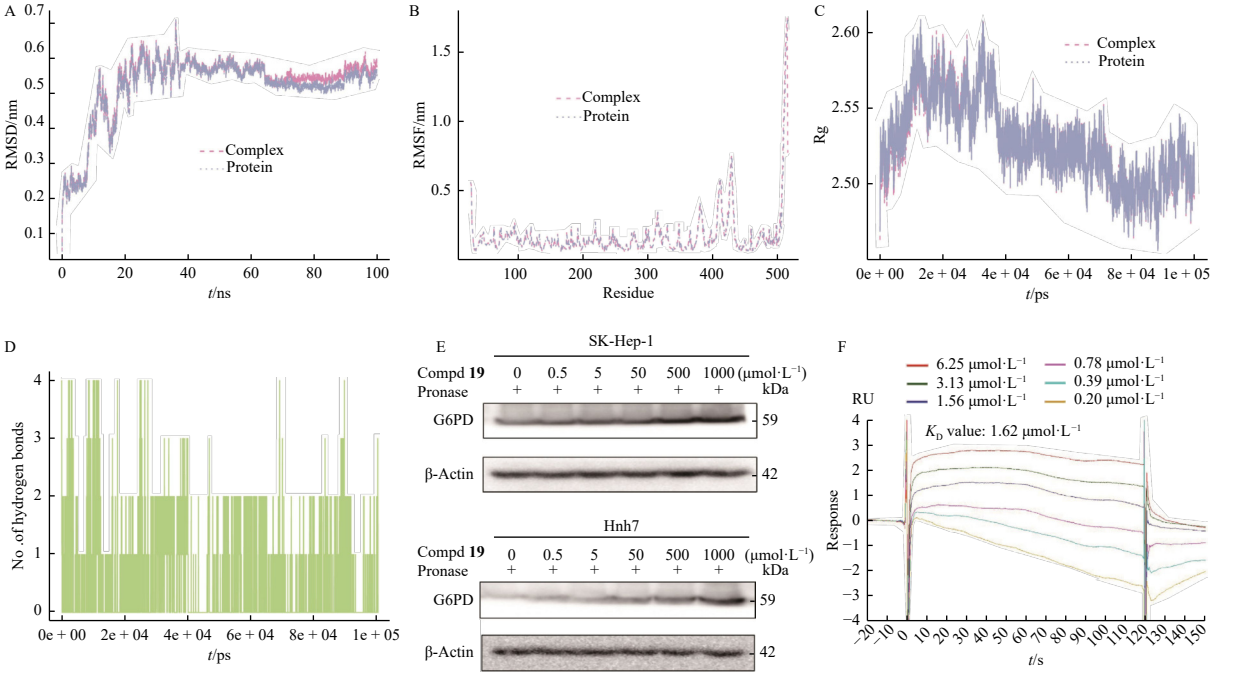


Fig. 4 Binding analysis of compound **19** to G6PD. (A) RMSD profiles of the free and complexed protein systems. (B) RMSF values of binding site residues. (C) Rg values for the free and complex protein systems. (D) Number of hydrogen bonds formed during simulation. (E) Dose-dependent stabilization of G6PD by compound **19** as determined by the DARTS assay. (F) Quantification of the interaction between compound **19** and G6PD *via* SPR.

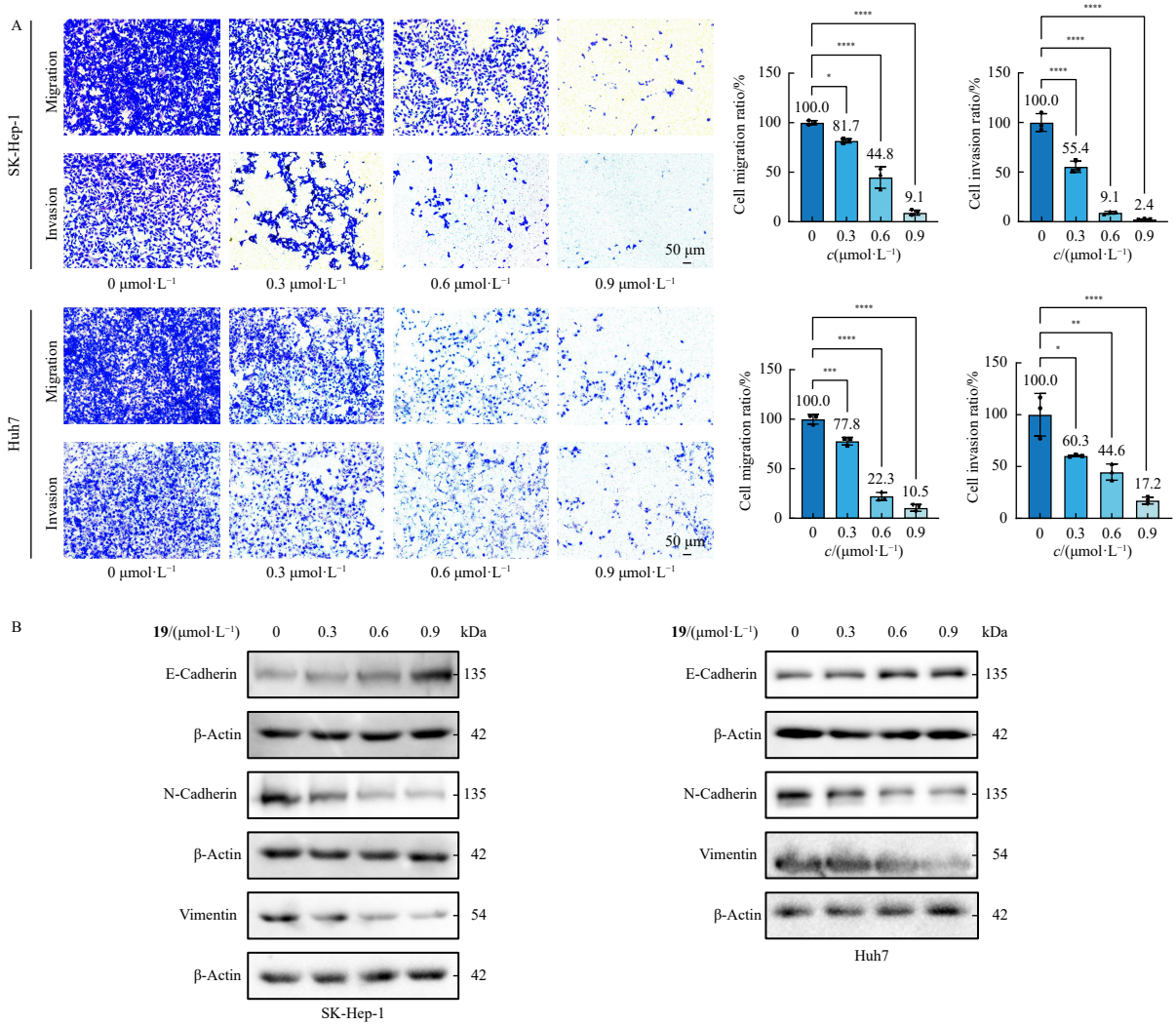


Fig. 5 Compound **19** inhibited the migration, invasion, and epithelial-mesenchymal transition (EMT) of SK-Hep-1 and Huh-7 cells. (A) Cell migration and invasion assays (n = 3). (B) Protein levels of *E*-cadherin, *N*-cadherin, and Vimentin. Data are presented as mean ± SD from three independent experiments. $^{*}P < 0.05$; $^{**}P < 0.01$; $^{***}P < 0.001$; $^{****}P < 0.0001$.

4. Experimental

4.1. Chemistry

4.1.1. General procedure for the synthesis of compounds **1–31** and **34–37**

Under an argon atmosphere, azide **A1** (136 mg, 0.5 mmol, 2.5 eq), (+)-sodium L-ascorbate (40 mg, 0.2 mmol, 1 eq), and $CuSO_4{\cdot}5H_2O$ (25 mg, 0.1 mmol, 0.5 eq) were dissolved in a mixture of THF (2 mL) and water (0.4 mL). The corresponding alkyne (0.2 mmol, 1.0 eq) was added, and the mixture was stirred at room temperature for 16 h. The reaction was quenched with saturated Na_2CO_3 solution and extracted with ethyl acetate (10 mL × 3). The combined organic phase was washed with water and saturated brine, then dried over anhydrous Na_2SO_4. The solvent was removed under reduced pressure, and the crude was purified by column chromatography (acetone–petroleum ether, 30∶70) to afford compounds **1**–**31** and **34**–**37**. Complete spectroscopic characterization data for compounds **1**–**31** and **34**–**37** are provided in the Supporting information.

4.1.2. Synthesis of compound **32**

A solution of compound **31** (13 mg, 0.02 mmol) in dichloromethane (0.5 mL) was treated with *m*-CPBA (85%, 3.8 mg, 0.02 mmol) at 0 °C. After stirring for 20 min, the reaction mixture was quenched with 10% aqueous $Na_2S_2O_3$, extracted with dichloromethane (3 × 5 mL). The combined organic extract was washed sequentially with saturated aqueous $NaHCO_3$ and brine, dried over anhydrous Na_2SO_4, filtered, and concentrated under reduced pressure. The residue was purified by silica gel column chromatography (acetone–petroleum ether, 30∶70) to afford compound **32** as a white solid (9 mg, 68% yield). (Spectral data of compound **32** are included in the Supporting information)

4.1.3. Synthesis of compound **33**

A solution of compound **31** (39 mg, 0.06 mmol) in dichloromethane (5 mL) was cooled to 0 ºC and treated with *m*-CPBA (85%, 20 mg, 0.12 mmol, 2.0 equiv). After stirring at 0 ºC for 20 min, the reaction mixture was allowed to warm to room temperature and stirred overnight. The reaction was quenched with 10% aqueous $Na_2S_2O_3$ and extracted with dichloromethane (3 × 15 mL). The combined organic extract was washed with water and brine, dried over anhydrous Na_2SO_4, filtered, and concentrated under reduced pressure. The residue was purified by silica gel column chromatography (acetone–petroleum ether, 30∶70) to afford compound **33** as a white solid (42 mg, 65% yield). Spectral data of compound **33** are included in the Supporting information.

4.2. Cell lines and cell culture

The detailed cell culture and MTT, CCK8 assay procedures

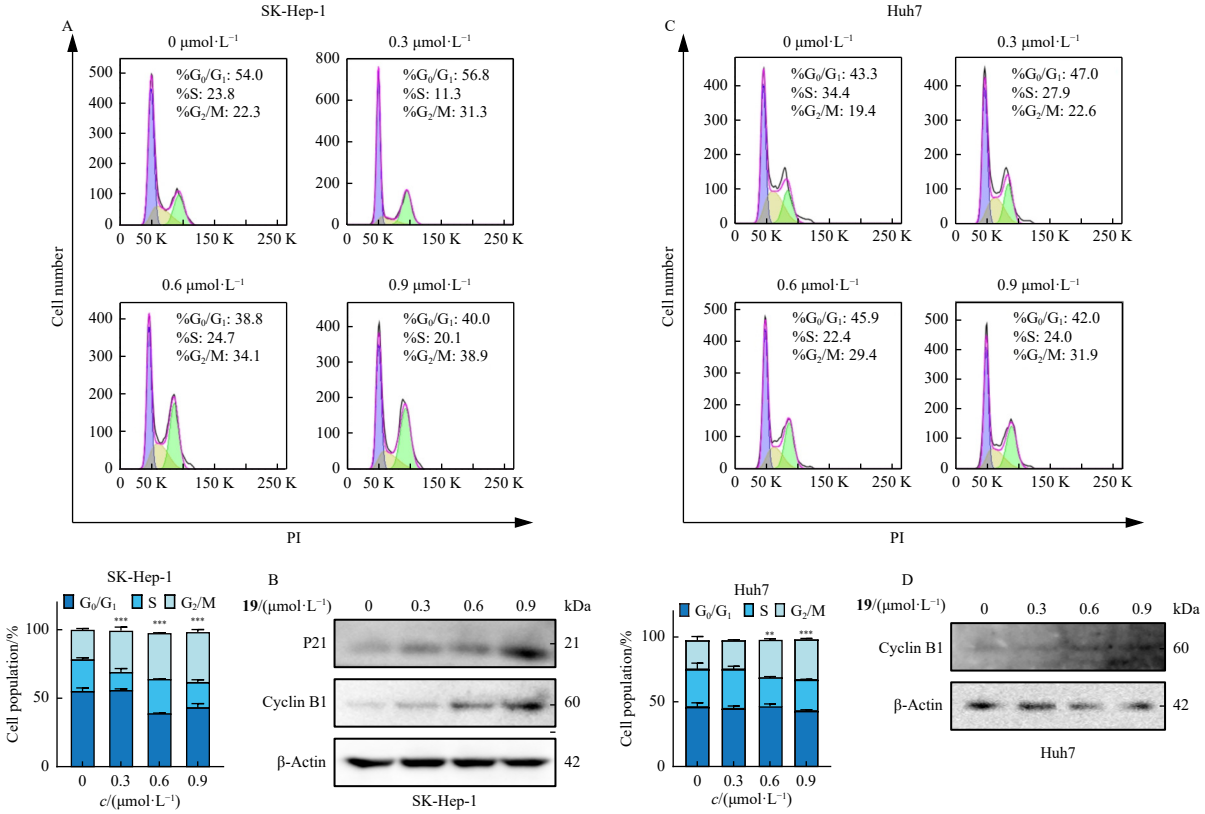


Fig. 6 Compound **19** induced G_2/M phase arrest in SK-Hep-1 and Huh-7 cells. (A, C) Flow cytometric analysis of the cell cycle in SK-Hep-1 and Huh7 (n = 3). (B, D) Expression levels of G_2/M-related proteins Cyclin B1 and p21. Data are presented as mean ± SD from three independent experiments. $^{**}P < 0.01$; $^{***}P < 0.001$.

were performed as previously described [12].

4.3. Colony-formation assay

SK-Hep-1 and Huh-7 cells were plated in 6-well plates at a density of 5 × 10^2 cells per well and maintained at 37 ºC with 5% CO_2. After incubation 96 h, the cells were exposed to compound **19** at concentrations of 0.0, 0.3, 0.6, and 0.9 μmol·L^{-1}. The medium was then removed and replaced with 2 mL of fresh medium every three days. Following 6 days of culture, the cells were washed twice with 1 mL PBS, fixed with 70% ethanol for 30 min, and again washed twice with PBS. The fixed cells were stained with 0.1% crystal violet (Solarbio, Cat. No. C8470, Beijing, China) for 30 min, after which the plates were air-dried. Colony formation in the entire well was quantified by scanning the plates and analyzing the images using ImageJ software (Version 1.53 t, National Institutes of Health, Bethesda, USA).

4.4. Bioinformatic analysis

The Top 50 potential targets of compound **19** were first predicted by CIPHEN. From this set, HCC-associated genes were identified by differential expression analysis (|log FC| > 1.2, adjusted P-value < 0.01) using the "limma" R package and Kaplan–Meier survival analysis *via* the "survminer" R package. This integrated approach revealed a subset of 15 predicted targets that were not only differentially expressed in HCC tissues but also significantly correlated with patient survival.

Molecular docking of compound **19** with the 15 candidate proteins was conducted with Schrödinger's Maestro (Schrödinger, Version 12.8, NY, USA). Protein structures from the PDB were optimized and energy-minimized using the Protein Preparation Wizard, while the ligand structure (SDF) was prepared with LigPrep. Potential binding sites were identified with the SiteMap tool. Docking simulations were then performed in standard precision (SP) mode to assess the binding interactions.

4.5. Drug affinity responsive target stability assay

Total cellular proteins were isolated from SK-Hep-1 cells with RIPA lysis buffer, and protein concentration was quantified using a bicinchoninic acid (Ncmbio, Cat. No. WB6501, Suzhou, China) assay kit. Aliquots of 250 μg protein were dispensed into 1.5 mL tubes and treated with either compound **19** (0–1000 μmol·L^{-1}) or DMSO as a control, followed by incubation at room temperature for 1 h. Subsequently, pronase (Roche, Cat. No. 10165921001, Basel, Switzerland) was introduced at a pronase-to-protein ratio of 1∶1000 to digest the proteins. The processed samples were then subjected to Western blot analysis.

4.6. Surface plasmon resonance (SPR) assay

The G6PD protein was purchased from Proteintech China (Cat. No. 81299, Wuhan, China). G6PD was diluted in sodium acetate buffer (pH 4.5) at 1 mg·mL^{-1} and covalently immobilized onto a CM5 sensor chip (Cytiva, Cat. No. 29104988, Marlborough, USA) using an Amine Coupling Kit (Cytiva, Cat. No. BR100050, Marlborough, USA). Compound **19** (ranging from 0.20 to 6.25 μmol·L^{-1} in PBS with 0.005% P20 and 5% DMSO) were injected over the chip surface to monitor association and dissociation. Sensorgram data were processed and analyzed using Biacore S200 Surface Plasmon Resonance (SPR) System (Cytiva, Marlborough, USA).

4.7. Western blot analysis

The expression levels of proteins associated with migration, apoptosis, and cell cycle progression were assessed by Western blot. SK-Hep-1 and Huh-7 cells were plated in 10 cm plates and exposed to different concentrations of compound **19** for 12–48 h. After treatment, cells were lysed with RIPA buffer to obtain total protein extracts, and protein concentrations were determined us-

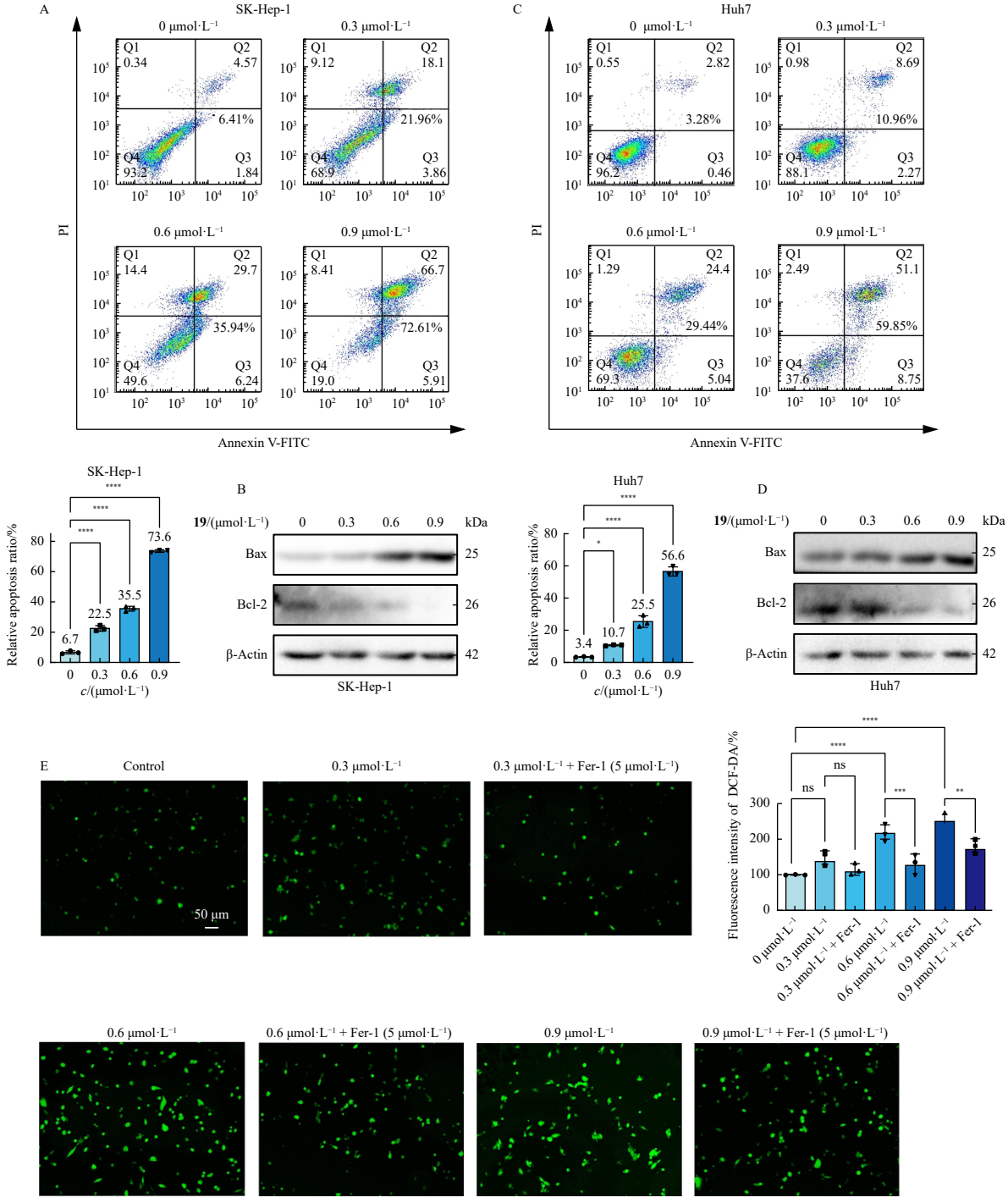


Fig. 7 Compound **19** induced apoptosis and ferroptosis in HCC cells. (A, C) Flow cytometric analysis of apoptosis in Huh-7 and SK-Hep-1 cells (n = 3). (B, D) Expression levels of apoptosis-related proteins Bax and Bcl-2. (E) Assessment of ROS production with or without Fer-1 pretreatment (n = 3). $^{*}P < 0.05$; $^{**}P < 0.01$; $^{***}P < 0.001$; $^{****}P < 0.0001$.

ing a BCA assay. Protein samples were separated by SDS-PAGE and subsequently transferred onto PVDF membranes (Millipore, Cat. No. IPV00010, Burlington, USA). The membranes were blocked and then probed with specific primary antibodies at 4 °C overnight, followed by incubation with an appropriate secondary antibody for 2 h at room temperature. Protein bands were visualized using an ECL solution (Tanon, Cat. No. 180-5001, Shanghai, China) and imaged with a multispectral imaging system (Sage Creation, Model No. SC680, Beijing, China).

4.8. Cell migration and invasion assay

Cell migration and invasion were evaluated using Transwell chambers. SK-Hep-1 and Huh-7 cells were seeded in the upper chambers at densities of 1×10^5 cells/mL and 5×10^4 cells/mL, respectively. For the migration assay, following adhesion, they were incubated for 24 h in serum-free DMEM supplemented with different concentrations of compound **19**. Non-migrated cells on the upper surface were then gently removed, while the migrated cells on the lower membrane were fixed with 70% ethanol and stained with 0.1% crystal violet for 30 min. Imaging was performed using an Olympus IX73 microscope (Olympus Corporation, Model No. IX73, Tokyo, Japan). For the invasion assay, the upper chambers were pre-coated with Matrigel matrix (BD Biosciences, Cat. No. 354234, Franklin Lakes, USA) diluted 1∶50 in ice-cold DMEM and allowed to solidify for 2 h before cell seeding. The

remaining procedures were consistent with those described for the migration assay.

4.9. Flow cytometry assay

The impact of compound **19** on cell cycle distribution and apoptosis of HCC cells was assessed by flow cytometry. SK-Hep-1 and Huh-7 cells were plated in 6 cm plates at 5×10^5 cells per well and exposed to increasing concentrations (0.0, 0.3, 0.6, and 0.9 μmol·L^{-1}) of compound **19** for 12 h (cell cycle analysis) or 48 h (apoptosis detection).

For cell cycle profiling, harvested cells were fixed in 70% ethanol at −20 °C overnight, then resuspended and stained in PBS containing 100 μg·mL^{-1} propidium iodide (BioFroxx, Cat. No. 1246MG010, Einhorn, Germany) and 200 μg·mL^{-1} RNase A (Solarbio, Cat. No. R1030, Beijing, China). Apoptosis was measured by resuspending cells in binding buffer and dual-staining with Annexin V-FITC and PI for 15 min in the dark. Data acquisition was performed using a BD Accuri C6 flow cytometer (BD Biosciences, Cat. No. 650643, San Jose, CA, USA).

4.10. Reactive oxygen species assay kit

SK-Hep-1 cells in the logarithmic growth phase were trypsinized and seeded into 96-well plates. A total of 100 μL of complete medium was added to each well, and the cells were incubated in a 37 °C, 5% CO_2 incubator for 24 h to allow adhesion (reaching approximately 60%–70% confluence) before compound **19** treatment. Compound **19** and ferrostatin-1 were diluted in complete medium, Fer-1 was administered 1 h prior to compound **19** treatment, and the cells were co-incubated for 12 h. According to the instructions of the Reactive Oxygen Species Assay Kit (Beyotime, Cat. No. S0033S, Shanghai, China), DCFH-DA was diluted at 1∶1000 to a final concentration of 10 μmol·L^{-1}. After removing the culture medium, an appropriate volume of the diluted DCFH-DA solution was added to each well. The plates were incubated at 37 °C for 30 min. Following three washes, the cells were observed and imaged using a fluorescence microscope.

Funding

This work was supported by the National Natural Science Foundation of China (Nos. 22137008 and 82473809), the Xingdian Yingcai Project (No. YNWR-KJLJ-2019-002), the Reserve Talents of Young and Middle-aged Academic and Technical Leaders in Yunnan Province (No. 202105AC160021), and the Yunnan Fundamental Research Projects (No. 202401AS070077).

Supporting information

NMR and MS data for compounds **1**–**37**, original figures of Western blot (PDF) can be requested by sending E-mail to the corresponding author.

Declaration of competing interest

These authors have no conflict of interest to declare.

References

1 Zheng J, Wang S, Xia L, et al. Hepatocellular carcinoma: signaling pathways and therapeutic advances. *Signal Transduct Target Ther*. 2025;10(1):35. https://doi.org/10.1038/s41392-024-02075-w.
2 Singh SP, Madke T, Chand P. Global epidemiology of hepatocellular carcinoma. *J Clin Exp Hepatol*. 2025;15(2):102446. https://doi.org/10.1016/j.jceh.2024.102446.
3 Asma ST, Acaroz U, Imre K, et al. Natural products/bioactive compounds as a source of anticancer drugs. *Cancers*. 2022;14(24):6203. https://doi.org/10.3390/cancers14246203.
4 Kim DY, Choi BY. Costunolide—a bioactive sesquiterpene lactone with diverse therapeutic potential. *Int J Mol Sci*. 2019;20(12):2926. https://doi.org/10.3390/ijms20122926.
5 Lin X, Peng Z, Su C. Potential anti-cancer activities and mechanisms of costunolide and dehydrocostuslactone. *Int J Mol Sci*. 2015;16(5):10888-10906. https://doi.org/10.3390/ijms160510888.
6 Vadaparthi PRR, Pavan KC, Kumar K, et al. Synthesis of costunolide derivatives by Pd-catalyzed heck arylation and evaluation of their cytotoxic activities. *Med Chem Res*. 2015;24(7):2871-2878. https://doi.org/10.1007/s00044-015-1337-5.
7 Srivastava SK, Abraham A, Bhat B, et al. Synthesis of 13-amino costunolide derivatives as anticancer agents. *Bioorg Med Chem Lett*. 2006;16(16):4195-4199. https://doi.org/10.1016/j.bmcl.2006.05.083.
8 Pavan KC, Devi A, Ashok YP, et al. "Click" reaction mediated synthesis of costunolide and dehydrocostuslactone derivatives and evaluation of their cytotoxic activity. *J Asian Nat Prod Res*. 2016;18(11):1063-1078. https://doi.org/10.1080/10286020.2016.1193012.
9 Su L, Zhang X, Ma Y, et al. New guaiane-type sesquiterpenoid dimers from *Artemisia atrovirens* and their antihepatoma activity. *Acta Pharm Sin B*. 2021;11(6):1648-1666. https://doi.org/10.1016/j.apsb.2020.12.006.
10 Su LH, Ma WJ, Ma YB, et al. Artemiprincepsolides A–F, novel germacrane-guaiane and eudesmane-guaiane sesquiterpenoid dimers from *Artemisia princeps* and their antihepatoma activity. *Chin J Chem*. 2023;41(20):2648-2656. https://doi.org/10.1002/cjoc.202300242.
11 Su LH, Ma WJ, Ma YB, et al. Artemiprinolides A–M, thirteen undescribed sesquiterpenoid dimers from *Artemisia princeps* and their antihepatoma activity. *Phytochemistry*. 2023;211:113714. https://doi.org/10.1016/j.phytochem.2023.113714.
12 He X, Ma W, Hu J, et al. Diverse structures and antihepatoma effect of sesquiterpenoid dimers from *Artemisia eriopoda* by AKT/STAT signaling pathway. *Signal Transduct Target Ther*. 2023;8(1):64. https://doi.org/10.1038/s41392-022-01267-6.
13 Gao Z, Ma WJ, Li TZ, et al. Artemidubolides A–T, cytotoxic unreported guaiane-type sesquiterpenoid dimers against three hepatoma cell lines from *Artemisia dubia*. *Phytochemistry*. 2022;202:113299. https://doi.org/10.1016/j.phytochem.2022.113299.
14 Dong W, Ma WJ, Ma YB, et al. Guaiane-type sesquiterpenoid dimers from *Artemisia zhongdianensis* and antihepatoma carcinoma activity *via* the p38MAPK pathway. *Chin J Chem*. 2023;41(19):2453-2468. https://doi.org/10.1002/cjoc.202300166.
15 Li TZ, Yang XT, Wang JP, et al. Biomimetic synthesis of lavandiolides H, I, and K and artematrolide F *via* Diels–Alder reaction. *Org Lett*. 2021;23(21):8380-8384. https://doi.org/10.1021/acs.orglett.1c03120.
16 Yan JX, Li QH, Li TZ, et al. Design and synthesis of guaianolide-germacranolide heterodimers as novel anticancer agents against hepatocellular carcinoma. *Drug Dev Res*. 2023;84(6):1285-1298. https://doi.org/10.1002/ddr.22087.
17 Janganati V, Ponder J, Jordan CT, et al. Dimers of melampomagnolide B exhibit potent anticancer activity against hematological and solid tumor cells. *J Med Chem*. 2015;58(22):8896-8906. https://doi.org/10.1021/acs.jmedchem.5b01187.
18 Ren H, Zhang YY, Li YL, et al. Semisynthesis and non-small-cell lung cancer cytotoxicity evaluation of germacrane-type sesquiterpene lactones from *Elephantopus scaber*. *J Nat Prod*. 2022;85(2):352-364. https://doi.org/10.1021/acs.jnatprod.1c00936.
19 Li TZ, Yang XT, Ma WJ, et al. Design, synthesis, and biological evaluation of artemyrianolide H derivatives as potential antihepatoma agents. *Bioorg Chem*. 2023;137:106617. https://doi.org/10.1016/j.bioorg.2023.106617.
20 Ding Y, Xue Q, Liu S, et al. Identification of parthenolide dimers as activators of pyruvate kinase M2 in xenografts of glioblastoma multiforme *in vivo*. *J Med Chem*. 2020;63(4):1597-1611. https://doi.org/10.1021/acs.jmedchem.9b01328.
21 Li TZ, Huang FD, Yan JX, et al. Discovery of dimeric guaianolides with all carbon linkers as potential antihepatoma agents. *Eur J Med Chem*. 2025;300:118160. https://doi.org/10.1016/j.ejmech.2025.118160.
22 de Sena MPP, Franco LS, Montagnoli TL, et al. Molecular hybridization: a powerful tool for multitarget drug discovery. *Expert Opin Drug Discov*. 2024;19(4):451-470. https://doi.org/10.1080/17460441.2024.2322990.
23 Xu Z, Zhao SJ, Liu Y. 1,2,3-Triazole-containing hybrids as potential anticancer agents: current developments, action mechanisms and structure-activity relationships. *Eur J Med Chem*. 2019;183:111700. https://doi.org/10.1016/j.ejmech.2019.111700.
24 Xiao Z, Gu Y, Dong H, et al. Strategic application of CuAAC click chemistry in the modification of natural products for anticancer activity. *Eur J Med Chem Rep*. 2023;9:100113. https://doi.org/10.1016/j.ejmcr.2023.100113.
25 Ding Y, Guo H, Ge W, et al. Copper(I) oxide nanoparticles catalyzed click chemistry based synthesis of melampomagnolide B-triazole conjugates and their anti-cancer activities. *Eur J Med Chem*. 2018;156:216-229. https://doi.org/10.1016/j.ejmech.2018.06.058.
26 Janganati V, Ponder J, Balasubramaniam M, et al. MMB triazole analogs are potent NF-κB inhibitors and anti-cancer agents against both hematological and solid tumor cells. *Eur J Med Chem*. 2018;157:562-581. https://doi.org/10.1016/j.ejmech.2018.08.010.
27 Khazir J, Hyder I, Gayatri JL, et al. Design and synthesis of novel 1,2,3-triazole derivatives of coronopilin as anti-cancer compounds. *Eur J Med Chem*. 2014;82:255-262. https://doi.org/10.1016/j.ejmech.2014.05.053.
28 Wang YC, Li TZ, Chen JJ. Compound-protein interaction prediction based on heterogeneous network reveals potential antihepatoma agents. *iScience*. 2024;27(8):110418. https://doi.org/10.1016/j.isci.2024.110418.
29 Meng Q, Zhang Y, Hao S, et al. Recent findings in the regulation of G6PD and its role in diseases. *Front Pharmacol*. 2022;13:932154. https://doi.org/10.3389/fphar.2022.932154.
30 Lu M, Lu L, Dong Q, et al. Elevated G6PD expression contributes to migration and invasion of hepatocellular carcinoma cells by inducing epithelial-mesenchymal transition. *Acta Biochim Biophys Sin (Shanghai)*. 2018;50(4):370-380. https://doi.org/10.1093/abbs/gmy009.
31 Zhang Z, Liew CW, Handy DE, et al. High glucose inhibits glucose-6-phosphate dehydrogenase, leading to increased oxidative stress and *β*-cell apoptosis. *FASEB J*. 2010;24(5):1497-1505. https://doi.org/10.1096/fj.09-136572.
32 Cao F, Luo A, Yang C. G6PD inhibits ferroptosis in hepatocellular carcinoma by targeting cytochrome P450 oxidoreductase. *Cell Signal*. 2021;87:110098. https://doi.org/10.1016/j.cellsig.2021.110098.